Journal of Atmospheric and Solar-Terrestrial Physics xxx (2017) 1–11

Contents lists available at ScienceDirect

Journal of Atmospheric and Solar-Terrestrial Physics

journal homepage: www.elsevier.com/locate/jastp

# Data-adaptive harmonic analysis and modeling of solar wind-magnetosphere coupling

Dmitri Kondrashov *, Mickaël D. Chekroun

*Department of Atmospheric and Oceanic Sciences, University of California, Los Angeles, United States*

ARTICLE INFO

*Keywords:*
Stochastic modeling
Solar wind
Magnetosphere
Auroral electrojet

ABSTRACT

The solar wind-magnetosphere coupling is studied by new data-adaptive harmonic decomposition (DAHD) approach for the spectral analysis and inverse modeling of multivariate time observations of complex nonlinear dynamical systems. DAHD identifies frequency-based modes of interactions in the combined dataset of Auroral Electrojet (AE) index and solar wind forcing. The time evolution of these modes can be very efficiently simulated by using systems of stochastic differential equations (SDEs) that are stacked per frequency and formed by coupled Stuart-Landau oscillators. These systems of SDEs capture the modes' frequencies as well as their amplitude modulations, and yield, in turn, an accurate modeling of the AE index' statistical properties.

## 1. Introduction

Empirical models have proven to be an important addition to understanding and predicting physical phenomena, largely due to the application of mathematical techniques which extract information of the variability of a system of which we do not fully understand the physical nature. In space physics, most historical empirical models have focused their attention on processes at or inside of geosynchronous orbit due, primarily, to the plethora of observations from geosynchronous, med-, and low-Earth orbit spacecraft, and recognition of harmful effects of relativistic energy radiation, such as deep-dielectric charging in spacecraft electrical components (Baker et al., 1987). The list of empirical models applied to model and understand the near-Earth space plasma is exhaustive. There are examples of the nearest-neighbor approaches for data-driven empirical magnetic field modeling (Sitnov et al., 2008), linear prediction (Baker and McPherron, 1990), statistical normalized mean (Kellerman and Shprits, 2012; Kellerman et al., 2013); neural networks (NN) (e.g. Koons and Gorney, 1991; Fukata et al., 2002; Ling et al., 2010; Zhelavskaya et al., 2016; Bortnik et al., 2016), and NARMAX (e.g Balikhin et al., 2011); while the Kalman filter data assimilation techniques may utilize linear (Kondrashov et al., 2007; Shprits et al., 2007, 2013; Daae et al., 2011; Kellerman et al., 2014; Merkin et al., 2016) and nonlinear methods (Kondrashov et al., 2011).

Broadly speaking, some of the more dynamically-oriented data-driven approaches such as and nonlinear autoregression moving average with exogenous inputs (NARMAX) and NN, can be associated with the *System Science* (Vassiliadis, 2006; Borovsky and Denton, 2014) and machine learning, where the evolution of the state of the complex dynamical system is represented by a time-dependent state vector composed of a relatively small number of relevant variables, and the laws evolution are learned or inferred from the simulations of the high-end models or observations.

Recently, Kondrashov et al. (2015) have introduced the Multilayer Stochastic Model (MSM) framework allowing for inferring a broad class of inverse models including the standard statistical ones. This approach relies on a formulation of inverse modeling as a *closure problem*, i.e. finding an *optimal model* that describes the evolution of partial observations of a complex high-dimensional dynamical system. The existence of such an optimal closure is guaranteed by the Mori-Zwanzig (MZ) formalism of statistical mechanics (Zwanzig, 2001; Chorin et al., 2002; Kondrashov et al., 2015). The MSM framework emphasizes the ubiquitous role of the triad of nonlinear, stochastic and memory effects in the derivation of data-driven closure models with good skill in simulating and predicting the main dynamical features, be it as an output of a high-end geophysical model or as a set of observations.

The solar wind–magnetosphere coupling occurs over wide range of spatial and temporal scales, and it has been studied extensively by various data-driven nonlinear dynamical techniques, such as time delay embedding, Singular Spectrum Analysis (SSA), and local-linear filters, for deterministic description of the global component of magnetospheric dynamics and statistical description of its multi-scale behavior (Ukhorskiy et al., 2002, 2004; Sitnov et al., 2000).

* Corresponding author.
*E-mail address:* dkondras@atmos.ucla.edu (D. Kondrashov).

https://doi.org/10.1016/j.jastp.2017.12.021
Received 9 May 2017; Received in revised form 23 December 2017; Accepted 30 December 2017
Available online xxxx
1364-6826/

This study demonstrates that in the context of the solar wind-magnetosphere coupling, an appropriate change of basis by application of the recent *Data-adaptive Harmonic Decomposition (DAHD)* technique introduced in (Chekroun and Kondrashov, 2017) allows us to reliably detect frequency-based interaction patterns between solar wind and Auroral Electrojet (AE) index; see Section 3. Furthermore, unlike previous efforts on stochastic modeling of AE that do not take into account external forcing by the solar wind (Pulkkinen et al., 2006; Anh et al., 2008), here we show that DAHD makes possible to perform successful stochastic modeling of AE index by a simple class of frequency-based MSMs —with few coefficients to estimate—namely the *multilayer Stuart-Landau models (MSLMs)* introduced in (Chekroun and Kondrashov, 2017); see Section 4.

## 2. Data

The Sun emits gigantic clouds of ionized gas (plasma) that propagate through the solar wind and eventually may hit magnetosphere. The interactions with the magnetosphere may result in a number of adverse effects that are collectively referred to as space weather. The location of Advanced Composition Explorer (ACE) and Wind spacecrafts at the Lagrange point L1 between the Earth and the Sun, about 1,500,000 km forward of Earth, enables these satellites to give up to 1 h advance warning of the arrival of damaging space weather events at Earth including severe geomagnetic disturbances. ACE satellite was launched in 1997 and Wind in 1994, respectively, and long history of high-resolution 1-min bow-shock-nose-shifted solar wind magnetic field and plasma data from these satellites have been compiled at OMNIWeb.

In this study we have used standard hourly averaged 2008–2013 datasets from the OMNIWEB database (http://omniweb.gsfc.nasa.gov) of solar wind parameters and interplanetary magnetic field (IMF), as well as Auroral Electrojet (AE) index that represents ground-based geomagnetic measurements. Furthermore, the small number of gaps during this period in solar wind and IMF were filled by SSA (Kondrashov et al., 2010, 2014).

For the analysis conducted below, we log-transformed and standardized the original *AE* index, namely by subtracting associated time series mean and divided by correspondent standard deviation. Various proxies for the solar wind forcing have been proposed by using nonlinear combinations of solar wind parameters and IMF (Burton et al., 1975; Perreault and Akasofu, 1978). By applying NARMAX, Boynton et al. (2011) have shown that the selection of solar wind–magnetosphere coupling function for best predictive capabilities of *Dst* index can be done objectively in a data-driven manner. To demonstrate capabilities of the proposed methodology in this study, we have chosen one of the proposed proxies, namely electric field parameter $V_{sw}B_z$ composed of solar wind velocity $V_{sw}$ and z-component of IMF $B_z$, and standardized it as well. The total length of the resulting dataset is $N = 44592$ points, and Fig. 1 shows selected time interval of 1 000 h corresponding to approximately 41 days of hourly data.

## 3. Frequency-based analysis of solar wind–AE coupling

The Data-adaptive Harmonic Decomposition (DAHD) (Chekroun and Kondrashov, 2017) is a signal processing technique that allows for a decomposition of the power and phase spectra via data-adaptive modes within a time-embedded phase space. Unlike other techniques exploiting time-embedding — such as M-SSA (Ghil et al., 2002) or nonlinear dimension reduction techniques (Gavrilov et al., 2016) — DAHD exploits a combination of integral operator and semigroup techniques (Engel and Nagel, 2006) that help decompose the original signal into elementary signals that as illustrated below, are narrowband for each separate discrete Fourier frequency, while being data-adaptive.

At a practical level, the key feature of the method relies on the construction of matrices that exploit cross-correlations in a different way than found in standard statistical methods, such as in Principal Component Analysis (PCA) (Preisendorfer, 1988); see Eq. (2) below. As explained by Chekroun and Kondrashov (2017) and discussed below, the eigenmodes associated with such matrices exhibit a data-adaptive feature that shows up in their phase rather than in their shape; see (8) below.

The mathematical details of the approach are provided in (Chekroun and Kondrashov, 2017) within a general framework, including the case of multivariate time series issued from a mixing dynamical system, either stochastic or deterministic. Central to the approach is the spectral analysis of a class of integral operators whose kernels are built from correlation functions. For the sake of simplicity, we recall first from (Chekroun and Kondrashov, 2017) how such an integral operator is constructed in the case of a one-dimensional time series $X(t)$. Given the two-sided autocorrelation function (ACF), $\rho$ (of $X(t)$), estimated on the interval $I = [-\tau/2, \tau/2]$, such an operator takes the form

$$\mathscr{L}_\rho(\Psi)(r) := \frac{1}{\tau}\left(\int_{-\frac{\tau}{2}}^{\frac{\tau}{2}-r}\rho(s+r)\Psi(s)\,\mathrm{d}s, + \int_{\frac{\tau}{2}-r}^{\frac{\tau}{2}}\rho(r+s-\tau)\Psi(s)\,\mathrm{d}s\right), \quad r \in I, \tag{1}$$

and acts on any square-integrable function $\Psi$ on the interval $I$. The parameter $\tau > 0$ characterizes the embedding window but is chosen in practice so that $\rho(t)$ has sufficiently decay over $[-\tau/2, \tau/2]$.

In practice, the discretization of the operator $\mathscr{L}_\rho$ defined by (1) leads to Hankel matrices built from temporal correlations in a different way than found in M-SSA (Ghil et al., 2002) and alike; see (2) below.

For multivariate time series, the ACF, $\rho$, is replaced by time-lagged cross-correlations, and operators such as given by (1) are grouped into a block operator whose discretization results into block-Hankel matrices; see (4) below and (Chekroun and Kondrashov, 2017; Sect. VI-D). The aforementioned DAH modes (DAHMs) are then obtained as eigenvectors of such a block-Hankel matrix, while the corresponding eigenvalues provide a notion of energy contained into the signal that although allowing for a reconstruction of the signal is not equivalent to variance; see (Chekroun and Kondrashov, 2017, Remark V.1-(ii)). We summarized hereafter the main properties of the spectral objects that the DAH methodology extracts from observations in a general context, before presenting results from the spectral analysis of the 2 -channel dataset of solar wind together with Auroral Electrojet (AE) index. In particular, we focus on:

(i) a multidimensional power spectrum, called the DAH power spectrum,
(ii) a multidimensional phase spectrum, called the DAH phase spectrum, and
(iii) the DAHMs.

### 3.1. DAH power spectrum, DAH phase spectrum and DAHMs

To determine these spectral elements, first we estimate from a given $d$-channel time series $\mathbf{X}(t_n) = (X_1(t_n), \ldots, X_d(t_n))$, with $n = 1, \ldots, N$, the two-sided cross-correlation coefficients $\rho_k^{(p,q)}$ between channels $p$ and $q$ at lag $k$ up to a maximum lag $M-1$, i.e. $-M+1 \le k \le M-1$.

As shown in (Chekroun and Kondrashov, 2017; Sect. VI-D), the discretization of the operator $\mathscr{L}_\rho$ given by (1) with $\rho = \rho^{(p,q)}$ leads to the following Hankel matrix $\mathbf{H}^{(p,q)}$,

$$\mathbf{H}^{(p,q)} = \begin{pmatrix} \rho_{-M+1}^{(p,q)} & \rho_{-M+2}^{(p,q)} & \cdots & \rho_0^{(p,q)} & \rho_1^{(p,q)} & \cdots & \rho_{M-1}^{(p,q)} \\ \rho_{-M+2}^{(p,q)} & \iddots & \iddots & \iddots & \iddots & \iddots & \rho_{-M+1}^{(p,q)} \\ \vdots & \iddots & \iddots & \iddots & \iddots & \iddots & \rho_{-M+2}^{(p,q)} \\ \rho_0^{(p,q)} & \iddots & \iddots & \iddots & \rho_{-M+1}^{(p,q)} & \iddots & \vdots \\ \rho_1^{(p,q)} & \iddots & \iddots & \iddots & \rho_{-M+2}^{(p,q)} & \iddots & \rho_0^{(p,q)} \\ \vdots & \rho_{M-1}^{(p,q)} & \rho_{-M+1}^{(p,q)} & \iddots & \iddots & \iddots & \vdots \\ \rho_{M-1}^{(p,q)} & \rho_{-M+1}^{(p,q)} & \rho_{-M+2}^{(p,q)} & \cdots & \rho_0^{(p,q)} & \cdots & \rho_{M-2}^{(p,q)} \end{pmatrix}. \tag{2}$$

Equivalently, this matrix can be viewed as a left-circulant matrix

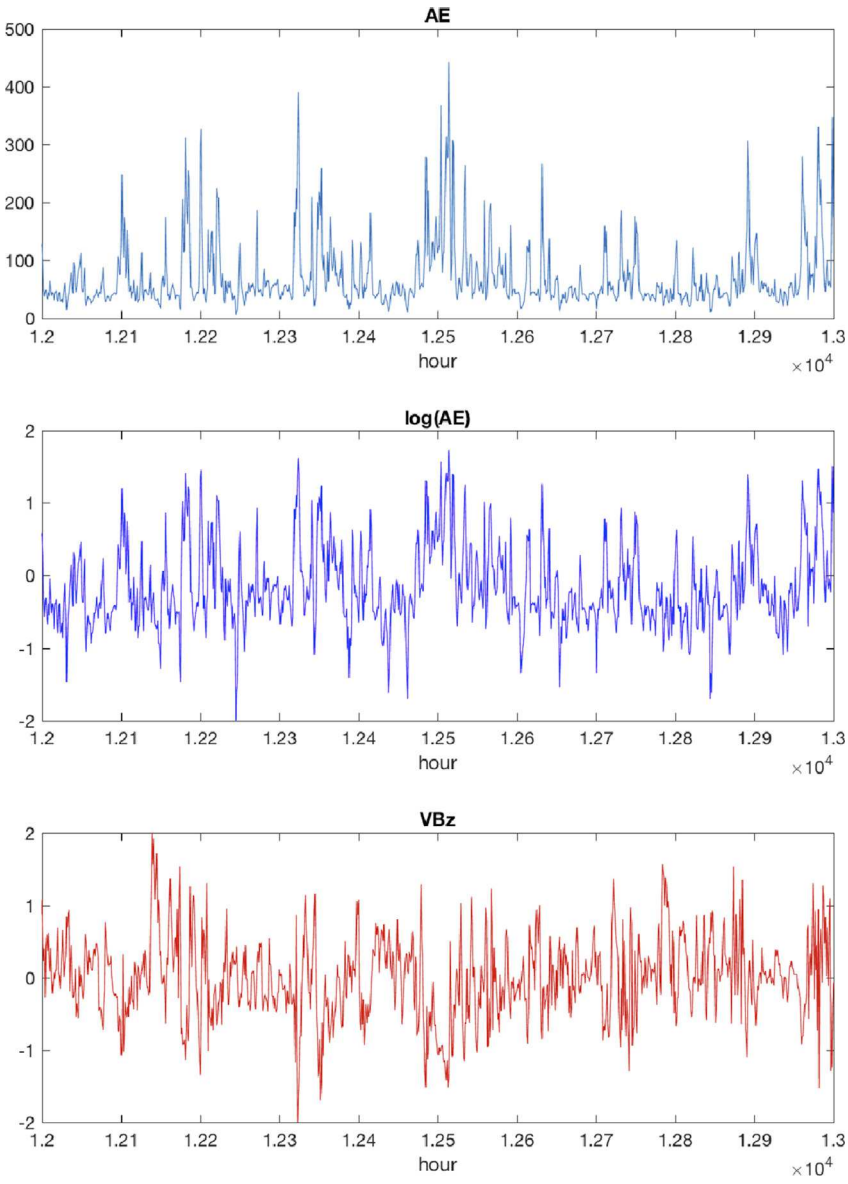


**Fig. 1.** Selected 1 000 h-long interval from 2008 to 2013 time series: upper panel – AE index; central panel – log-transformed and standardized AE index; lower panel – standardized solar wind forcing $V_{sw}Bz$, see text for details.

formed from the $(2M-1)$-dimensional row $\mathbf{r} = (\rho_{-M+1}^{(p,q)}, \cdots, \rho_0^{(p,q)}, \cdots, \rho_{M-1}^{(p,q)})$, i.e.:

$$\mathbf{H}^{(p,q)} = I - \mathrm{circ}\left(\rho_{-M+1}^{(p,q)}, \cdots, \rho_{-1}^{(p,q)}, \rho_0^{(p,q)}, \rho_1^{(p,q)} \cdots, \rho_{M-1}^{(p,q)}\right); \tag{3}$$

in other words, the rows of $\mathbf{H}^{(p,q)}$ are obtained by successive shifts to the left by one position, starting from $\mathbf{r}$ as a first row.

As mentioned above, by forming such a Hankel matrix for each $(p,q)$ in $\{1,\cdots,d\}^2$, one can assemble the following block-Hankel matrix $\mathfrak{C}$ constituted of $d^2$ blocks of size $(2M-1)\times(2M-1)$, each given according to

$$\begin{array}{l} \mathfrak{C}^{(p,q)} = \mathbf{H}^{(p,q)}, \text{ if } 1 \le p \le q \le d, \\ \mathfrak{C}^{(p,q)} = \mathbf{H}^{(q,p)}, \text{ else.} \end{array} \tag{4}$$

Note that because each of its building block, $\mathbf{H}^{(p,q)}$, is symmetric, and because $\mathfrak{C}^{(p,q)} = \mathfrak{C}^{(q,p)}$, the grand matrix $\mathfrak{C}$ is itself symmetric. Hereafter we use $M' = 2M-1$ for concision, reindexing the string $\{-M+1,\cdots,M-1\}$ to run from 1 to $M'$ as necessary.

(Chekroun and Kondrashov, 2017; Theorem V.1) provides then a useful characterization of the eigenvalues of $\mathfrak{C}$. It shows that the corresponding eigenvalues come in pairs of eigenvalues of opposite sign that can be grouped per Fourier frequency, and are actually given, at each frequency, as the singular values of a cross-spectral matrix depending on the data.

We recall from (Chekroun and Kondrashov, 2017) the main details concerning this latter property. First, denoting by $\widehat{\rho^{p,q}}(f)$ the Fourier transform at the Frequency $f$ of the cross-correlation function $\rho^{p,q}$, we consider the following $d\times d$ **cross-spectral matrix** $\Im(f)$ whose entries are given by

$$\Im_{p,q}^{k} = \begin{cases} \widehat{\rho^{q,p}}(f) \text{ if } q \ge p, \\ \widehat{\rho^{q,p}}(f) \text{ if } q < p. \end{cases} \tag{5}$$

Then (Chekroun and Kondrashov, 2017; Theorem V.1) shows that for

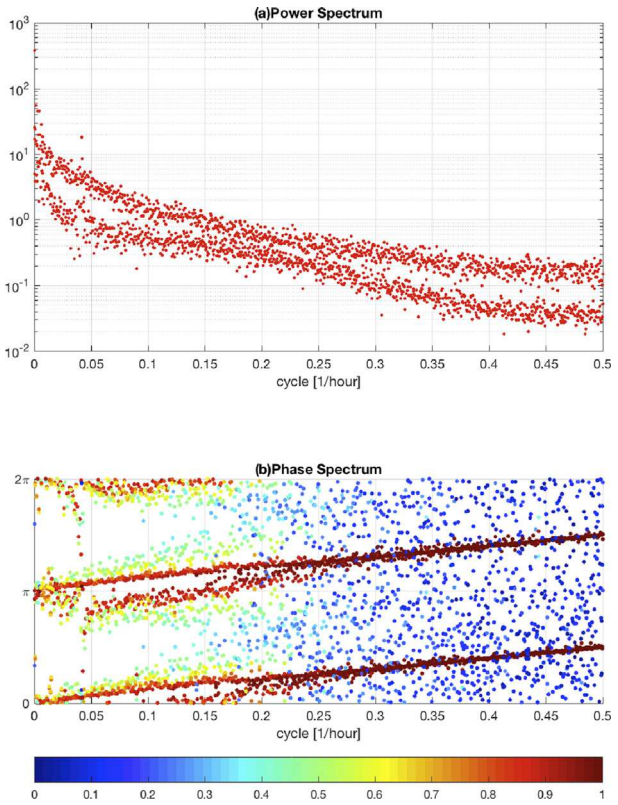


**Fig. 2.** (a) **Power and (b) phase DAH specra** for combined dataset of $V_{sw}B_z$ and $\log(AE)$ in Fig. 1. The color in phase spectrum indicates Euclidean norm of associated DAHM snippets, see text for details. (For interpretation of the references to color in this figure legend, the reader is referred to the Web version of this article.)

each **singular value** $\sigma_k(f)$ **of** $\Im(f)$ there exists, when $f \neq 0$, a pair of negative-positive eigenvalues $(\lambda^k_-(f), \lambda^k_+(f))$ of $\mathfrak{C}$ such that

$$\lambda^k_+(f) = -\lambda^k_-(f) = \sigma_k(f), \quad 1 \leq k \leq d, \tag{6}$$

i.e. $2d$ eigenvalues are associated with each Fourier frequency $f \neq 0$. The same theorem shows that $d$ (but not paired) eigenvalues are associated with the frequency $f = 0$.

Another key property identified by (Chekroun and Kondrashov, 2017; Theorem V.1) is that the eigenvectors of $\mathfrak{C}$, i.e. the aforementioned DAHMs, can also be grouped per Fourier frequency in an even more explicit fashion. Indeed (Chekroun and Kondrashov, 2017; Theorem V.1) shows that the eigenvectors of $\mathfrak{C}$ possess the following representation

$$\mathbf{W}_j = \left(\mathbf{E}^j_1, \cdots, \mathbf{E}^j_d\right)^{\mathrm{tr}}, \tag{7}$$

where each $\mathbf{E}^j_k$ is a $M'$-dimensional row vector that is explicitly associated with a Fourier frequency $f$ according to

$$\mathbf{E}^j_k(s) = B^j_k \cos\left(fs + \theta^j_k\right), \quad 1 \leq s \leq M', \tag{8}$$

where the amplitudes $B^j_k$ and the phases $\theta^j_k$ are both data-dependent, for each $1 \leq k \leq d$. According to this representation, each DAHM has thus a temporal (embedding) component with $s$ ranging from 1 to $M'$, and a spatial one with $k$ ranging from 1 to $d$, and since $\mathfrak{C}$ is symmetric, the collection of DAHMs form an orthogonal set. We will sometimes refer to a DAHM snippet, an $M'$-long segment $\mathbf{E}^j_k$ that arises in the representation (7) of a DAHM.

From (8) we can, given a Fourier frequency,

$$f_\ell = \frac{2\pi(\ell - 1)}{M' - 1}, \ \ell = 1, \cdots, \frac{M' + 1}{2}, \tag{9}$$

determine the following subset of indices in $\{1, \cdots, dM'\}$:

$$\mathscr{J}(f_\ell) := \{j \ : \ \text{s.t. (8) holds with} f = f_\ell\}. \tag{10}$$

Note that for reasons similar to those mentioned above, $\mathscr{J}(f_\ell)$ is composed of $2d$ indices when $\ell \neq 0$ and of $d$ indices if $\ell = 0$ such that the $\mathscr{J}(f_\ell)$'s form a partition of the total set of indices, $\{1, \cdots, dM'\}$.

Due to the simple form (8) of a DAHM snippet $\mathbf{E}^j_k$, the determination of the subset $\mathscr{J}(f_\ell)$ can be obtained by various means, for example by computing numerically the power spectral density $p^j_k$ of $\mathbf{E}^j_k$ and grouping the $j$'s for which the average power spectral density, $d^{-1}\sum_{k=1}^d p^j_k$, exhibits a dominant peak at the frequency $f_\ell$.

While formula (6) is useful for interpretation, it is not used numerically in practice. Instead, the eigenvalues of the $dM' \times dM'$ matrix $\mathfrak{C}$ are computed directly, and listed as the set of eigenvalues $(\lambda_j)_{1 \leq j \leq dM'}$. This is where the grouping of indices obtained by the procedure described above is used in practice. It allows indeed for a rearrangement of these eigenvalues per Fourier frequency (without having to form the cross-spectral matrix $\Im(f)$ for each frequency) into a useful object called the **DAH power spectrum**. The latter consists of forming, for each $\ell$ ranging from 1 to $(M' + 1)/2$, the discrete set

$$\mathscr{S}_\ell := \left\{\left|\lambda_j\right|, \ : \ j \in \mathscr{J}(f_\ell)\right\}, \tag{11}$$

or in other words, the collection of the $\mathscr{P}_\ell$ for $\ell$ ranging from 1 to $(M' + 1)/2$, denotes the DAH power spectrum that is evenly spaced in frequency (see Eq. (9)).

Fig. 2a shows the computed DAH power spectrum —with the $\left|\lambda_j\right|$'s plotted as red filled circles—for the two ($d = 2$) combined anomaly time series, namely $\log(AE)$ and $V_{sw}B_z$ (see Fig. 1) and an embedding parameter $M = 1000$ hours; the number of frequency bins in the Nyquist interval $N_f = (M' + 1)/2 = 1000$. There are exactly two pairs of DAHMs at each equidistant frequency $f$, except at $f = 0$, where there are two single (i.e. unpaired) modes. The DAH spectrum has more power in the low-frequency band and there is a pronounced peak at the 1-day periodicity, i.e. $f = 1/24 \approx 0.04$.

As explained in (Chekroun and Kondrashov, 2017; Sect. V), the DAH decomposition does not only provide a data-adaptive power spectrum but it also yields a well-defined DAH phase spectrum:

$$\Phi^j_k(f_\ell) := \arg\left(\lambda_j \widehat{\mathbf{E}}^j_k(f_\ell)\right) - \arg\left(\overline{\widehat{\mathbf{E}}^j_k(f_\ell)}\right), \tag{12}$$

where $\arg(z)$ denotes the *principal value* (that we adopt to lie in $[0, 2\pi)$ here) of the argument of the complex number $z$, while $\widehat{\mathbf{E}}^j_k$ and $\overline{\widehat{\mathbf{E}}^j_k}$ denote respectively the discrete Fourier transform of the DAHM snippet, $\mathbf{E}^j_k$, and its conjugate. The **DAH phase spectrum** is then obtained as the collection of the following discrete set,

$$\mathbf{\Phi}_\ell := \left\{\Phi^j_k(f_\ell) \ : \ j \in \mathscr{J}(f_\ell)\right\}, \tag{13}$$

as $\ell$ varies in from 1 to $(M' + 1)/2$.

Another useful property concerns the pair of DAHMs associated with a pair of DAH eigenvalues $(\lambda_j, \lambda_{j'})$, such that $\lambda_{j'} = -\lambda_j$ and $j$ and $j'$ thus belong to the same subset $\mathscr{J}(f)$. For such a DAHM pair, the theory shows indeed that their corresponding phases satisfy $\theta^{j'}_k = \theta^j_k + \pi/2$, i.e. in each DAHM pair the modes are shifted by one fourth of the period; see (Chekroun and Kondrashov, 2017; Theorem IV.1). These DAHMs are thus always in exact phase quadrature, as for a sine-and-cosine pair in

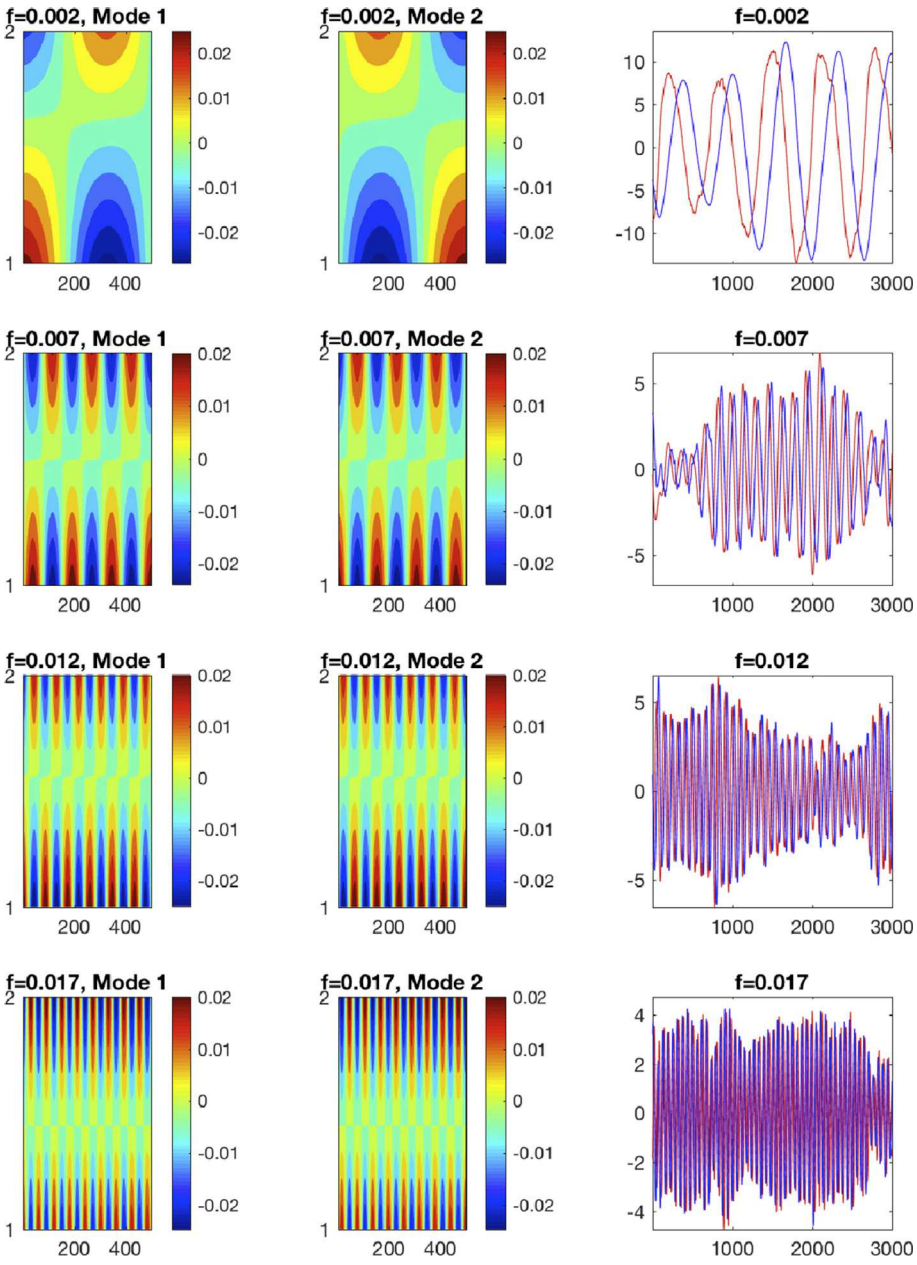


**Fig. 3. Left and center panels** — spatio-temporal patterns of the DAH mode (DAHM) pairs corresponding to the peak of the DAH power spectrum, i.e. to the largest $|\lambda_j|$ at the given temporal frequency $f$, cf. Fig. 2; in each panel, the $x$-axis is lag in hours, while the $y$-axis is the index of data channel: 1 – log($AE$), 2–$V_{sw}Bz$. The color bar represents DAHM amplitude. **Right panels** — associated DAH coefficients (DAHCs), with time in hours on the abscissa; see text for details. (For interpretation of the references to color in this figure legend, the reader is referred to the Web version of this article.)

Fourier analysis, but in a data-adaptive fashion as encapsulated in the $\theta_k^j$'s and the $B_k^j$'s; see Figs. 3 and 4 for an illustration.

Fig. 2b shows computed DAH phase spectrum $\mathbf{\Phi}_\ell$, which is color coded with information on the Euclidean norm of respective DAHM snippets $\left|\mathbf{E}_k^j(f_\ell)\right|$, that can be unambiguously associated with the $\Phi_k^j(f_\ell)$. Taking into account this phase-quadrature property, there are, for the dataset at hand, in total $d^2 = 4$ independent phase values $\Phi_k^j(f_\ell)$ given by DAHphase per frequency $f_\ell$. Three main features are clearly visible in this spectrum: (i) two straight lines, (ii) two "tongues" containing very few or no values in a low-frequency band with periodicities of larger than $\approx 4$ hours, and (iii) a diffuse background at higher frequencies. Moreover, the "tongues" areas are surrounded by regions of higher density than in the diffuse background, and the largest magnitudes of DAHM snippets are found in the regions of high density around the "tongues" and the straight lines.

To assess the dynamical relevance of these phase spectrum features, it is instructive to analyze results for the AE index combined with a (standardized) white noise instead of the solar wind forcing. The resulting DAH phase spectrum is shown in Fig. 5b, and as one can observe, the tongues surrounded by high-density regions are no longer apparent, while the largest magnitudes of DAHM snippets are strictly confined to two straight lines. Such result can be explained from the characterization of the DAH eigenvalues as singular values of the cross-spectral matrix, $\mathfrak{S}(f)$, with entries given in (5): since the white noise is by definition independent from the AE index at all lags, the off-diagonal terms are in theory equal to zero for each frequency $f$. In such a case, the theory (Chekroun and Kondrashov, 2017) predicts that the DAH spectrum is composed of two independent spectra associated with each of the (univariate) time series, and that the corresponding phase spectrum exhibits a linear dependence with $f$, such as seen in Fig. 5b. Moreover, the presence of the diffuse background in Fig. 5b is due to the finite length of time series resulting into the presence of small, but non-zero off-diagonal terms in the corresponding cross-spectral density matrix.

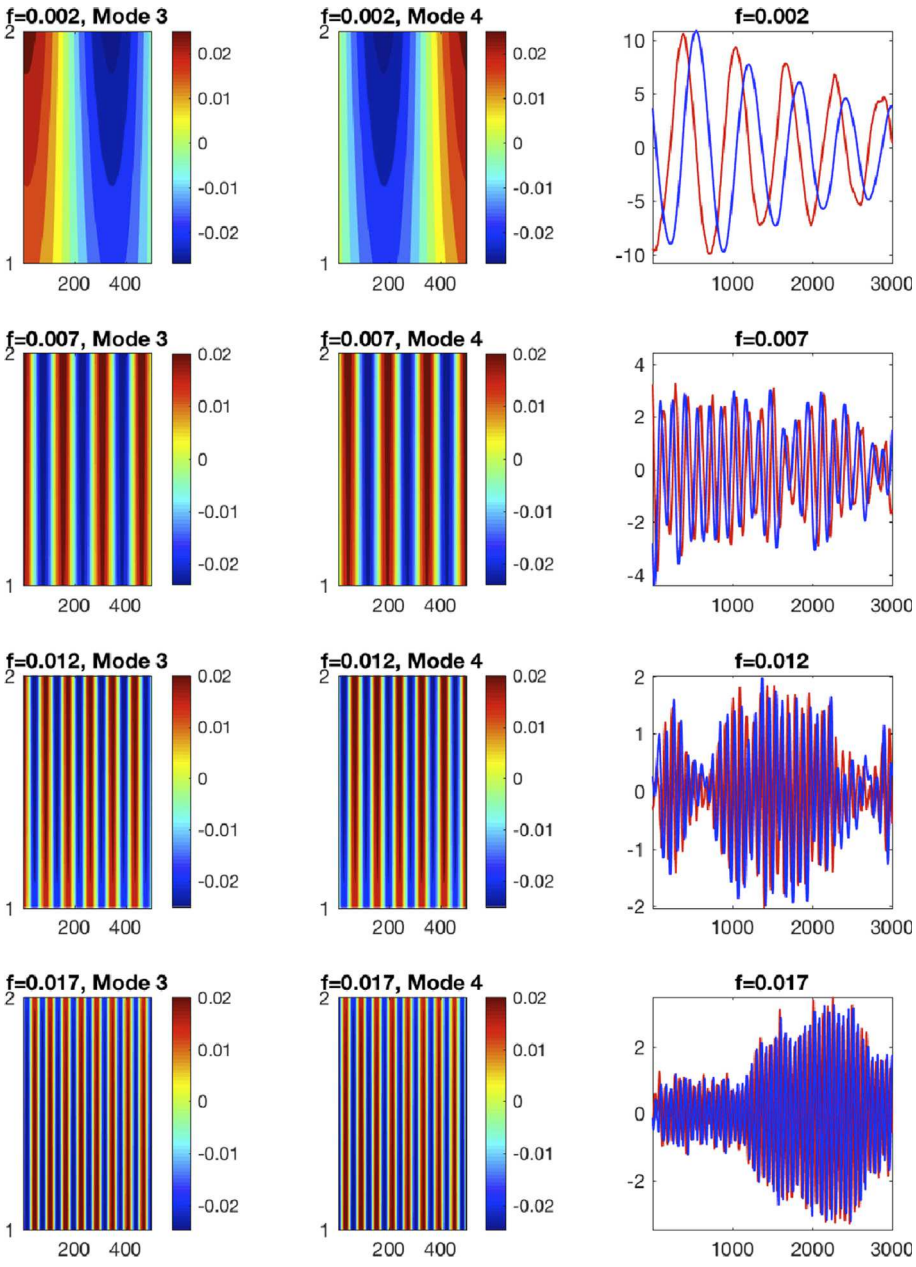


**Fig. 4.** Similar to Fig. 3, but for DAH mode pairs at the bottom of the power spectrum at a given frequency, i.e. with smallest $|\lambda_j|$.

The comparison with the white noise experiment thus strongly suggests that the presence of void tongues surrounded by high-density regions in Fig. 2b, is due to dynamical solar wind–magnetosphere interactions that are most pronounced at (relatively) low frequencies, where most of the energy is contained in both the AE index and solar wind forcing; see Fig. 2a. On the other hand, the absence of such structures at higher frequencies (and lower energy) indicates a weaker coupling, same as in the case of the white noise experiment.

The spatio-temporal patterns of the DAHMs at low frequencies are shown in the left and center columns of Figs. 3 and 4, and are visualized by exploiting the representation (7). More precisely, given a frequency $f$ of interest and a DAHM, $W_j$, associated with this frequency, we extract $d$ DAHM snippets, $\mathbf{E}_p^j$, each of length $M'$, and we form the array in which each row for $1 \leq p \leq d$, is given by $\mathbf{E}_p^j(s)$ when $s$ varies from 1 to $M'$; the index $p$ referring to channels and $s$ to (embedding) time. The resulting "spatio-temporal" array with $d$ rows and $M'$ columns gives thus a natural way to visualize a $dM'$-dimensional DAHM. The DAHMs are always in phase-quadrature, except at zero frequency.

The DAHM patterns show details of frequency-based information about the solar wind–magnetosphere interactions. For instance, the dominant variability patterns (Fig. 3) at a given $f$ — i.e. those corresponding to the pair with largest $|\lambda_j(f)|$ — inform us about the out-of-phase or time-lagged relationship existing at this frequency between the underlying time series. Furthermore, the amplitudes of these DAHMs for each frequency are roughly equal in each channel, i.e. in channel 1 corresponding to $\log(AE)$, and in channel 2 corresponding to $V_{sw}B_z$. On the other hand, DAHMs associated with the smallest $|\lambda_j(f)|$ have also their amplitude roughly equal in each channel, but exhibit an in-phase relationship; see left and center columns of Fig. 4.

In contrast, the DAHM patterns for the white noise experiment do not share such features. In particular, the pattern amplitudes are negligible in channels 2 and 1, for the largest (Fig. 6) and smallest $|\lambda_j(f)|$ (Fig. 7), respectively. This is another manifestation that in this case, the DAH

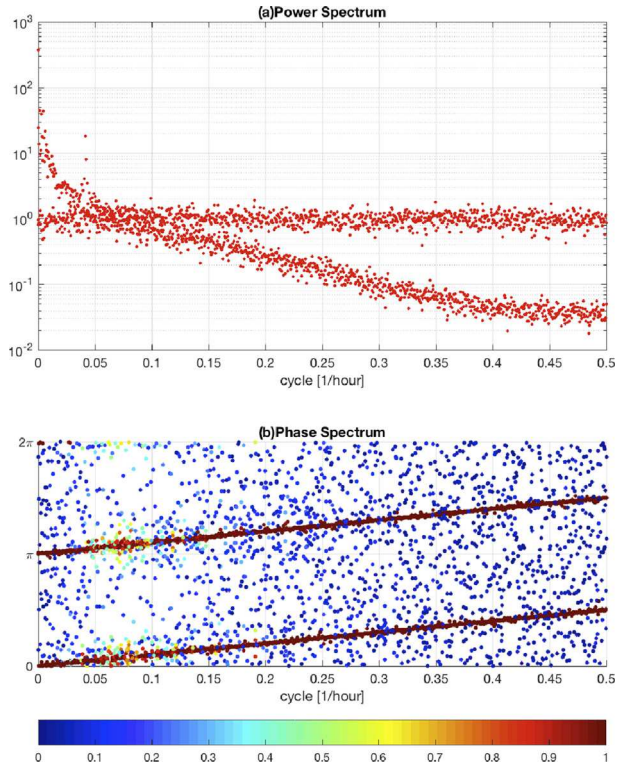


**Fig. 5.** Same as in Fig. 2, but when the white noise is used instead of solar wind forcing $V_{sw}B_z$.

power spectrum is composed of two independent univariate spectra, and that the energy contained in the AE index (i.e. channel 1) is substantially larger for $f \leq 0.017$ than in white noise (i.e. channel 2), see Fig. 5a.

### 3.2. DAH coefficients (DAHCs)

By analogy with M-SSA (Ghil et al., 2002), the multivariate dataset $\mathbf{X}$ can be projected onto the orthogonal set formed by the $\mathbf{W}_j$'s, in order to obtain the following **DAH expansion coefficients (DAHCs)**:

$$\xi_j(t) = \sum_{s=1}^{M'} \sum_{k=1}^{d} X_k(t+s-1)\mathbf{E}_k^j(s), \tag{14}$$

where $t$ varies from 1 to

$$N' = N - M' + 1. \tag{15}$$

Although the DAHCs are not formally orthogonal in time, the DAHC pair $(\xi_j(t), \xi_{j'}(t))$ associated with a DAHM pair $(\mathbf{W}_j, \mathbf{W}_{j'})$, is made of time series that are *nearly in phase quadrature*; a property that is all the more pronounced when the embedding parameter $M$ can be sufficiently large to resolve the decay of temporal correlations contained in $\mathbf{X}$; see Chekroun and Kondrashov (2017). In other words, the larger $M$ (subject to the length of the record), the more apparent is the phase quadrature between a pair of DAHCs associated with the same frequency.

For the dataset at hand, the panels of the right column of Figs. 3 and 4 show several DAHC pairs, $(\xi_j(t), \xi_{j'}(t))$, that account for the narrow-band temporal information contained at the characteristic frequency associated with the respective DAHM pair $(\mathbf{W}_j, \mathbf{W}_{j'})$. The latter pairs are shown in the left and center columns of these two figures, respectively, and as mentioned above, they exhibit a shift of, a quarter of a period in time. As one can see, the phase-quadrature property of the DAHCs is also satisfied sufficiently well, which bodes well for the success of the stochastic-modeling approach described in the next section.

Finally, we mention that any subset $\mathbf{B}$ of the set $\boldsymbol{\xi}$ of DAHCs, as well as the full set $\boldsymbol{\xi}$ itself, can be convolved with its corresponding set of DAHMs, $\mathbf{W}_j$, to produce a partial or full reconstruction of the original dataset, respectively. Thus, the following $j$th **reconstructed component (RC)** at time $t$ and for channel $k$ is defined as:

$$R_k^j(t) = \frac{1}{M_t} \sum_{s=L_t}^{U_t} \xi_j(t-s+1)\mathbf{E}_k^j(s),\ 1 \leq s \leq M', \tag{16}$$

where $L_t$ (resp. $U_t$) is a lower (resp. upper) bound in $\{1, \cdots, M'\}$, that is allowed to depend on time. The normalization factor $M_t$ equals $M'$, except near the ends of the time series, as in M-SSA (Ghil et al., 2002), and the sum of all the RCs recovers the original time series. The next section addresses the modeling of the $\xi_j$'s in (16), while the latter formula will be used to emulate the original dataset from the simulation of the DAHCs.

## 4. Stochastic modeling of the *AE* index

### 4.1. Inverse stochastic multilayer Stuart-Landau models (MSLM)

Chekroun and Kondrashov (2017) have shown how to leverage DAH decomposition to simplify the data-driven modeling effort into elemental multilayer stochastic models (MSMs) (Kondrashov et al., 2015) stacked per frequency. Given a sequence of partial observations issued from a dynamical system, the DAHCs allow one to recast these observations so as to model them within a universal parametric family of simple stochastic models, provided, roughly speaking, that the window $M$ is sufficiently large to resolve the decay of temporal correlations of a given dataset.

First, we consider a DAHC pair $(\xi_j(t), \xi_{j'}(t))$ associated with a pair of DAH eigenvalues $(\lambda_j, \lambda_{j'})$, such that $\lambda_{j'} = -\lambda_j$ with $j$ and $j'$ that belong thus to the same subset $\mathscr{J}(f)$ associated with a frequency $f$. Hereafter, we assume the time $t$ to be a continuous parameter. For such a DAHC pair, we form the complex time series, $\zeta_j(t) = \xi_j(t) + i\xi_{j'}(t)$ where $i^2 = -1$. Recalling from Sec. 3.2, that a DAHC pair $(\xi_j(t), \xi_{j'}(t))$ is constituted of narrowband time series that are nearly in phase quadrature, Chekroun and Kondrashov (2017) have shown that Stuart-Landau (SL) oscillators driven by an additive noise (Zakharova et al., 2016; Selivanov et al., 2012), represents a natural class of models to emulate the behavior of $\xi_j(t)$ and $\xi_{j'}(t)$:

$$\dot{z} = (\mu + i\gamma)z - (1 + i\beta)|z|^2 z + \varepsilon_t,\ \ z \in \mathbb{C}\,. \tag{17}$$

where $\mu, \gamma$ and $\beta$ are real parameters and $\varepsilon_t$ is a noise term, not necessarily white.

With the appropriate parameter values of $\mu, \gamma$ and $\beta$ as well as noise characteristics of $\varepsilon_t$, one can generate a solution $z(t)$ of (17) whose real and imaginary parts are also nearly in phase quadrature, modulated in amplitude and narrowband about the frequency $f$. As a consequence, it is reasonable to envision a good approximation of the complex DAHC $\zeta_j(t)$ by $z(t)$, when numerically solving (17).

On the other hand, particular pair $(\xi_j(t), \xi_{j'}(t))$ is not isolated from the other DAHC pairs associated with the same frequency $f$, and their collective behavior must be taken into account. The natural idea consists then of introducing an appropriate dynamical coupling between the corresponding individual SL oscillators to reproduce any global phase coherence that would be displayed by the DAHC pairs at a given frequency, as well as to take into account the associated temporal and spatial cross-pair correlations in the noise term $\varepsilon_t$.

The MSM framework of (Kondrashov et al., 2015) is particularly suited to deal with these issues, and when applied to (17), it leads to multilayer Stuart-Landau models (MSLMs) such as introduced in Chekroun and Kondrashov (2017). In the simplest case of one layer used to model the noise $\varepsilon_t$, and by denoting $(x_j(t), y_j(t))$ variables as numerical approximation of the DAHC pair $(\xi_j(t), \xi_{j'}(t))$ associated with a frequency $f = f_\ell$, the resulting MSLM is given by the following system of SDEs:

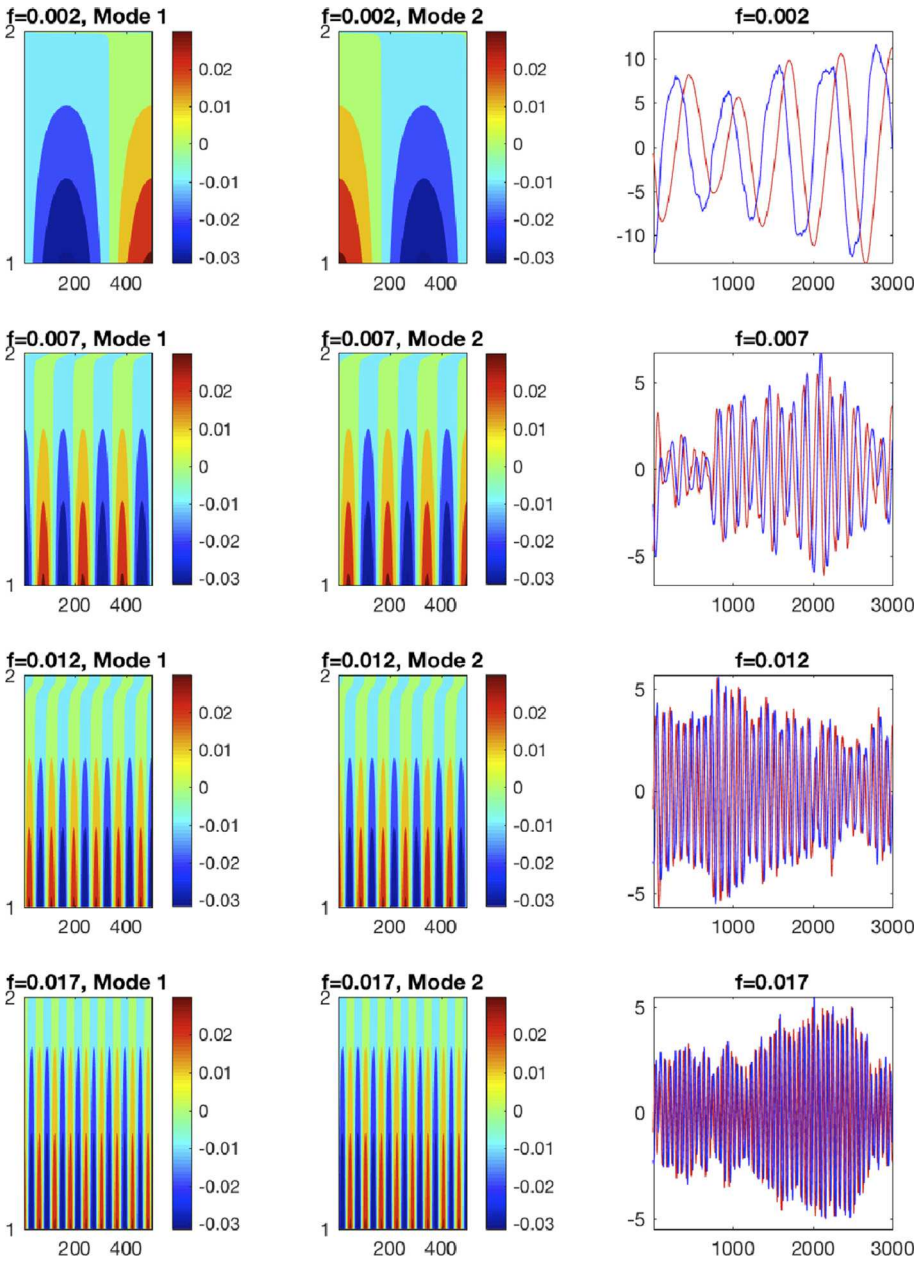


**Fig. 6.** Same as in Fig. 3, but when the white noise is used instead of solar wind forcing $V_{sw}B_z$.

$$
\begin{aligned}
\dot{x}_j &= \beta_j(f)x_j - \alpha_j(f)y_j + \sigma_j(f)x_j\left(x_j^2+y_j^2\right) + \\
&\quad \sum_{\substack{i\neq j \\ i\in \mathcal{F}_d(f)}} b_{ij}^x(f)x_i + \sum_{\substack{i\neq j \\ i\in \mathcal{F}_d(f)}} a_{ij}^x(f)y_i + \varepsilon_j^x, \\
\dot{y}_j &= \alpha_j(f)x_j + \beta_j(f)y_j + \sigma_j(f)y_j\left(x_j^2+y_j^2\right) + \\
&\quad \sum_{\substack{i\neq j \\ i\in \mathcal{F}_d(f)}} a_{ij}^y(f)x_i + \sum_{\substack{i\neq j \\ i\in \mathcal{F}_d(f)}} b_{ij}^y(f)y_i + \varepsilon_j^y, \\
\dot{\varepsilon}_j^x &= L_{11}^j(f)x_j + L_{12}^j(f)y_j + M_{11}^j(f)\varepsilon_j^x + M_{12}^j(f)\varepsilon_j^y + \qquad (MSLM) \\
&\quad Q_{11}^{ij}(f)\dot{W}_1^j + Q_{12}^{ij}(f)\dot{W}_2^j + \sum_{\substack{i\neq j \\ i\in \mathcal{F}_d(f)}} \sum_{k=1}^{2} Q_{1k}^{ij}(f)\dot{W}_k^j, \\
\dot{\varepsilon}_j^y &= L_{21}^j(f)x_j + L_{22}^j(f)y_j + M_{21}^j(f)\varepsilon_j^x + M_{22}^j(f)\varepsilon_j^y + \\
&\quad Q_{21}^{ij}(f)\dot{W}_1^j + Q_{22}^{ij}(f)\dot{W}_2^j + \sum_{\substack{i\neq j \\ i\in \mathcal{F}_d(f)}} \sum_{k=1}^{2} Q_{2k}^{ij}(f)\dot{W}_k^j.
\end{aligned}
\tag{18}
$$

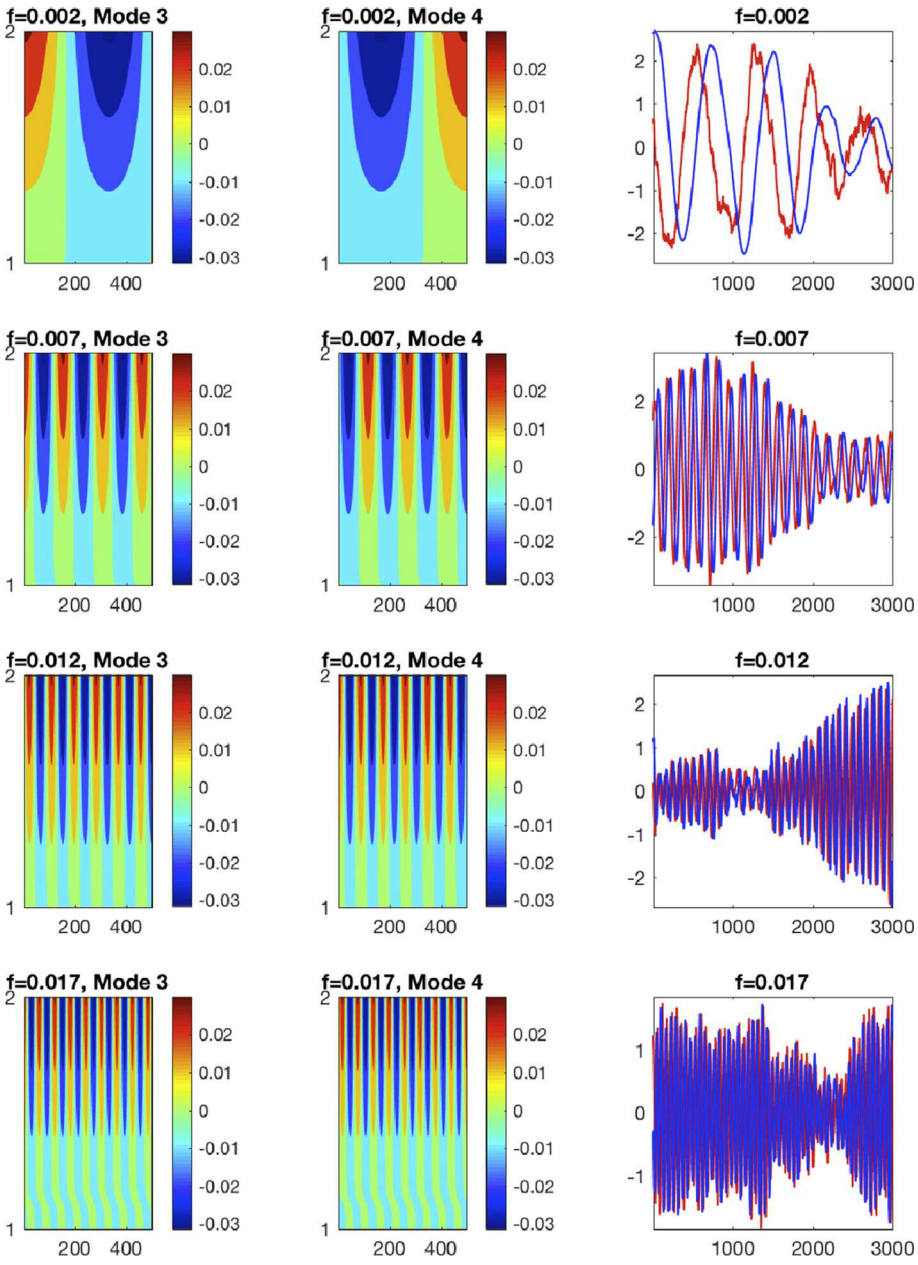


**Fig. 7.** Same as in Fig. 4, but when the white noise is used instead of solar wind forcing $V_{sw}B_z$.

where index $j$ varies thus in the subset of indices, $\mathscr{J}_d(f_\ell)$, constituted by the indices of $\mathscr{J}(f)$ (given by 10) which correspond to $d$ distinct pairs. The $W_k^j$'s with $k=1$ or $k=2$, and $1 \le j \le d$, form $2d$ independent Brownian motions. The sums in the $\varepsilon_j^x$- and $\varepsilon_j^y$-equations take into account correlations between the pairs, at the noise level. Note that for $f \equiv 0$, there are exactly $d$ modes that are not paired, and they are modeled by a linear MSM, as in (Kondrashov et al., 2015).

Following Kondrashov et al. (2015), all model coefficients are estimated starting from the main level of MSLM for each $(x_j, y_j)$-pair, namely by successive multiple linear regression (MLR). As needed, extra layers in an MSLM can be added until the regression residuals at the last layer are reasonably approximated by a white noise, according to the stopping criterion described in (Kondrashov et al., 2015; Appendix A). For the $log(AE)$ modeling presented in Sec. 4.2, the optimal model has the form as shown in Eq. (*MSLM*), i.e. with just one extra layer for $\varepsilon_t$ variable. This extra MSLM layer allows for coping with complex state-dependencies — such as dependence on the past of $x_j(t)$ and $y_j(t)$ — as well as with temporal correlations exhibited by the residual, $\varepsilon_t$, of the main layer for the $x_j$- and $y_j$-variables; see (Kondrashov et al., 2015; Proposition 3.3).

Because the SL oscillators are uncoupled across the frequencies, the DAH-MSLM approach is computationally quite efficient and, moreover, totally parallelizable in practice. Indeed, the model coefficients can be estimated in parallel for each frequency, i.e. by successive pairwise regressions with linear constraints on $\alpha_j(f), \beta_j(f)$ and $\sigma_j(f)$. These constraints impose the necessary model structure in Eq. (*MSLM*) for each $(x_j, y_j)$-pair, namely antisymmetry for the linear part without coupling terms, as well as equal and nonpositive values $\sigma_j(f) \le 0$ to ensure asymptotic stability.

Moreover, the DAH-MSLMs are also run in parallel across the frequencies, being driven by the same white-noise realization in the last model layer; this driving noise serving thus of dynamical mechanism for the coupling between different frequencies. Simulated DAHCs are then convolved with DAHMs according to (16) to obtain the **harmonic reconstruction component (HRC)** consisting of the sum of the RCs associated with a same Fourier frequency $f$:

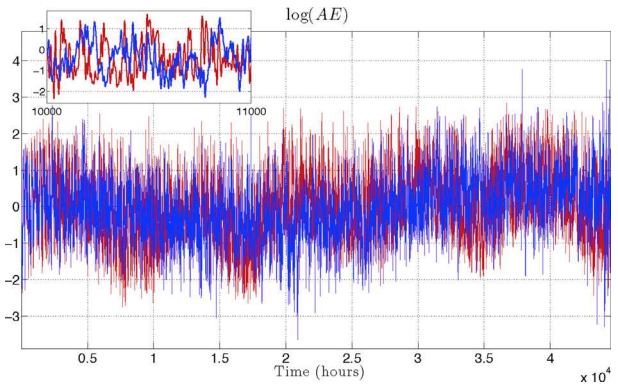


**Fig. 8. Time series of** log($AE$)**:** red – measured, blue – random stochastic realization of the DAH-MSLM model. (For interpretation of the references to color in this figure legend, the reader is referred to the Web version of this article.)

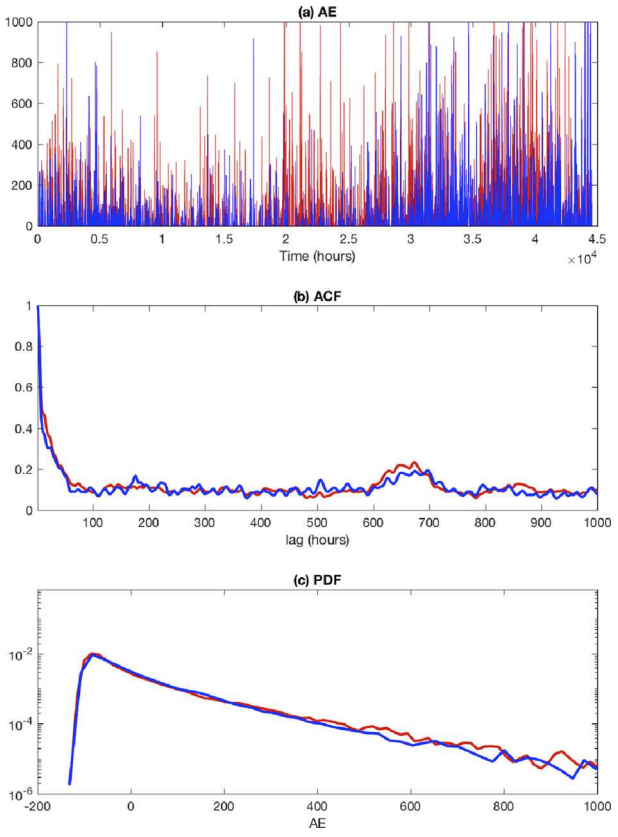


**Fig. 9. Comparison of statistical properties of measured and modeled AE.** (a) *AE* for red – measured and blue – random stochastic realization of the DAH-MSLM model; (b) Autocorrelation function (ACF); (c) Probability density function (PDF) (the mean has been removed). (For interpretation of the references to color in this figure legend, the reader is referred to the Web version of this article.)

$$R_k(t;f) = \sum_{j\in\mathcal{J}(f)} R_k^j(t), \tag{19}$$

where $\mathcal{J}(f)$ denotes the set of indices given by (10). Summing the HRCs over the frequencies that lie within a frequency band of interest allows us thus to model that particular frequency band.

### 4.2. DAH-MSLM of the AE index

In this section we demonstrate inverse modeling skills obtained by applying DAH-MSLM approach to the dataset composed of the log($AE$)-index combined with solar wind forcing (see Sec. 2). In a first step, the DAHCs (Sec. 3.2) are computed using DAHD results for an embedding window of $M = 1000$ hours (i.e. $M' = 1999$) (Sec. 3.1). In a second step, a collection of such DAHCs is modeled—for a frequency band of interest—by using the MSLM approach described above. The simulated log($AE$)-index is then obtained from HRCs (Eq. (19)). The overall number of independent coefficients in MSLM is small and fixed for each $(x_j, y_j)$-pair, e.g. the main layer of Eq. Main_syst involves estimation of $3 + 4(d-1) = 7$ coefficients from $2N' = 2(44592 - 1000 + 1) = 87186$ DAH-processed observations, over the full time interval 2008–2013.

Fig. 8 shows a stochastic realization of log($AE$) index, as simulated by the DAH-MSLM model in the frequency band $f \leq 0.1 hour^{-1}$ that accounts for most of the variance, and where according to the DAH phase spectrum, the dynamical coupling with the solar wind is most pronounced, see Fig. 2b and Sec. 3.1. The DAH-MSLM model was estimated and simulated in parallel for different frequencies (see Sec. 4), taking in total $\approx$ 1min of CPU time on a 4-core 2.9 GHz Intel Core i7 MacBook Pro laptop. The comparison with the measured log($AE$) (in the same frequency band) is meant to be qualitative and statistical due to stochastic nature of the DAH-MSLM model. After back-transformation, Fig. 9a shows that the multiplicity of abrupt variations, quiet episodes of variable durations as well as their punctuation by burst episodes of different magnitudes are all well reproduced in simulated *AE*. In addition, the model captures reasonably well long-term amplitude modulation over 2008–2013.

Furthermore, Fig. 9b and c demonstrate excellent modeling skill by DAH-MSLM in reproducing key statistical properties of the back-transformed *AE* index (Fig. 9a), such as autocorrelation functions (ACFs) and probability density functions (PDFs). The DAH-MSLM captures very well not only the decay of ACF, but also its 27–day peak (solar rotation) and 1-day modulations (Fig. 9b), as well as the highly nonlinear skewed PDF shape (Fig. 9c). The obtained results show high fidelity of DAH-MSLM approach since the logarithmic scale requires high accuracy in the modeling to resolve the multiplicity of abrupt variations spanning several orders of magnitude. Preliminary results also indicate that inclusion of solar-wind forcing in DAH-MSLM modeling is important to reproduce heavy tails in PDF of *AE*; the detailed study of using presented approach to isolate internal vs. externally forced magnetospheric variability is left for the future work.

## 5. Concluding remarks

The recent DAH-MSLM approach of (Chekroun and Kondrashov, 2017) has been successfully applied to identify frequency-based patterns of dynamical interaction between the *AE* index and the solar wind forcing, as well as to produce an accurate inverse modeling of key statistical properties of the *AE* index. Future work will extend the presented approach into a prediction context and will include other proxies of solar wind forcing and geomagnetic indices, as well as other space physics datasets and higher sampling frequency. We believe that the presented approach could also be useful to identify frequency-based content of internal magnetospheric variability as opposed from the one caused by external solar forcing.

## Acknowledgements

The authors would like to thank the anonymous reviewers for their useful comments that helped improved the presentation of this article. This study was facilitated in part by the 3rd "International Symposium on Recent Observations and Simulations of the Sun-Earth System (ISROSES-

III)" 11–16 September 2016, Varna, Bulgaria. This research was supported by grant N00014-16-1-2073 from the Multidisciplinary University Research Initiative (MURI) of the Office of Naval Research, and by the National Science Foundation grants OCE-1243175, OCE-1658357 and DMS-1616981.

## Appendix A. Supplementary data

Supplementary data related to this article can be found at https://doi.org/10.1016/j.jastp.2017.12.021.

## References

Anh, V.V., Yong, J.M., Yu, Z.G., 2008. Stochastic modeling of the auroral electrojet index. J. Geophys. Res.: Space Pol. 113, A10215.

Baker, D.N., McPherron, R.L., 1990. Extreme energetic particle decreases near geostationary orbit: a manifestation of current diversion within the inner plasma sheet. J. Geophys. Res. 95, 6591–6599.

Baker, D., Belian, R., Klebasadel, H.P.R., B. J.B., R.W., 1987. Deep dielectric charging effects due to high-energy electrons in earth's outer magnetosphere. J. Electrost. 20, 3–19.

Balikhin, M.A., Boynton, R.J., Walker, S.N., Borovsky, J.E., Billings, S.A., Wei, H.L., 2011. Using the NARMAX approach to model the evolution of energetic electrons fluxes at geostationary orbit. Geophys. Res. Lett. 38.

Borovsky, J.E., Denton, M.H., 2014. Exploring the cross correlations and autocorrelations of the ULF indices and incorporating the ULF indices into the systems science of the solar wind-driven magnetosphere. J. Geophys. Res. 119, 4307–4334.

Bortnik, J., Li, W., Thorne, R.M., Angelopoulos, V., 2016. A unified approach to inner magnetospheric state prediction. J. Geophys. Res. 121, 2423–2430.

Boynton, R.J., Balikhin, M.A., Billings, S.A., Wei, H.L., Ganushkina, N., 2011. Using the narmax ols-err algorithm to obtain the most influential coupling functions that affect the evolution of the magnetosphere. J. Geophys. Res.: Space Pol. 116, A05218.

Burton, R.K., McPherron, R.L., Russell, C.T., 1975. An empirical relationship between interplanetary conditions and dst. J. Geophys. Res. 80, 4204–4214.

Chekroun, M.D., Kondrashov, D., 2017. Data-adaptive harmonic spectra and multilayer Stuart-Landau models. Chaos 27, 093110. https://doi.org/10.1063/1.4989400.

Chorin, A.J., Hald, O.H., Kupferman, R., 2002. Optimal prediction with memory. Physica D 166, 239–257.

Daae, M., Shprits, Y.Y., Ni, B., Koller, J., Kondrashov, D., Chen, Y., 2011. Reanalysis of radiation belt electron phase space density using various boundary conditions and loss models. Adv. Space Res. 48.

Engel, K.-J., Nagel, R., 2006. A Short Course on Operator Semigroups. Springer Science & Business Media.

Fukata, M., Taguchi, S., Okuzawa, T., Obara, T., 2002. Neural network prediction of relativistic electrons at geosynchronous orbit during the storm recovery phase: effects of recurring substorms. Ann. Geophys. 20, 947–951.

Gavrilov, A., Mukhin, D., Loskutov, E., Volodin, E., Feigin, A., Kurths, J., 2016. Method for reconstructing nonlinear modes with adaptive structure from multidimensional data. Chaos: An Interdisciplinary Journal of Nonlinear Science 26, 123101.

Ghil, M., Allen, M.R., Dettinger, M.D., Ide, K., Kondrashov, D., Mann, M.E., Robertson, A.W., Saunders, A., Tian, Y., Varadi, F., Yiou, P., 2002. Advanced spectral methods for climatic time series. Rev. Geophys. 40, 1003.

Kellerman, A.C., Shprits, Y.Y., 2012. On the influence of solar wind conditions on the outer-electron radiation belt. J. Geophys. Res. 117.

Kellerman, A.C., Shprits, Y.Y., Turner, D.L., 2013. A geosynchronous radiation – belt electron empirical prediction (GREEP) model. Space Weather 11, 463–475.

Kellerman, A.C., Shprits, Y.Y., Kondrashov, D., Subbotin, D., Makarevich, E., Donovan, R.A., Nagai, T., 2014. 3D data assimilation and reanalysis of radiation belt electrons: observations of a 4-zone structure using five spacecraft and the VERB code. J. Geophys. Res. Space Physics 119, 8764–8783. https://doi.org/10.1002/2014JA020171.

Kondrashov, D., Shprits, Y., Ghil, M., Thorne, R., 2007. A kalman filter technique to estimate relativistic electron lifetimes in the outer radiation belt. J. Geophys. Res. 112.

Kondrashov, D., Shprits, Y., Ghil, M., 2010. Gap filling of solar wind data by singular spectrum analysis. Geophys. Res. Lett. 37, 15101.

Kondrashov, D., Ghil, M., Shprits, Y., 2011. Lognormal kalman filter for assimilating phase space density data in the radiation belts. Space Weather 9, S11006.

Kondrashov, D., Denton, R., Shprits, Y.Y., Singer, H.J., 2014. Reconstruction of gaps in the past history of solar wind parameters. Geophys. Res. Lett. 41, 2702–2707.

Kondrashov, D., Chekroun, M.D., Ghil, M., 2015. Data-driven non-Markovian closure models. Physica D 297, 33–55.

Koons, H.C., Gorney, D.J., 1991. A neural network model of the relativistic electron flux at geosynchronous orbit. J. Geophys. Res. 96, 5549–5556.

Ling, A.G., Ginet, G.P., Hilmer, R.V., Perry, K.L., 2010. A neural network – based geosynchronous relativistic electron flux forecasting model. Space Weather 8.

Merkin, V.G., Kondrashov, D., Ghil, M., Anderson, B.J., 2016. Data assimilation of low-altitude magnetic perturbations into a global magnetosphere model. Space Weather 14, 165–184, 2015SW001330.

Perreault, P., Akasofu, S., 1978. A study of geomagnetic storms. Geophys. J. Int. 54, 547–573.

Preisendorfer, R.W., 1988. Principal Component Analysis in Meteorology and Oceanography. Elsevier, New York, p. 425.

Pulkkinen, A., Klimas, A., Vassiliadis, D., Uritsky, V., 2006. Role of stochastic fluctuations in the magnetosphere-ionosphere system: a stochastic model for the ae index variations. J. Geophys. Res.: Space Pol. 111, A10218.

Selivanov, A.A., Lehnert, J., Dahms, T., Hövel, P., Fradkov, A.L., Schöll, E., 2012. Adaptive synchronization in delay-coupled networks of Stuart-Landau oscillators. Phys. Rev. E 85, 016201.

Shprits, Y., Kondrashov, D., Chen, Y., Thorne, R., Ghil, M., Friedel, R., Reeves, G., 2007. Reanalysis of relativistic radiation belt electron fluxes using CRRES satellite data, a radial diffusion model, and a Kalman filter. J. Geophys. Res. 112.

Shprits, Y., Kellerman, A., Kondrashov, D., Subbotin, D., 2013. Application of a new data operator-splitting data assimilation technique to the 3-D VERB diffusion code and CRRES measurements. Geophys. Res. Lett. 40, 4998–5002.

Sitnov, M.I., Sharma, A.S., Papadopoulos, K., Vassiliadis, D., Valdivia, J.A., Klimas, A.J., Baker, D.N., 2000. Phase transition-like behavior of the magnetosphere during substorms. J. Geophys. Res.: Space Pol. 105, 12955–12974.

Sitnov, M.I., Tsyganenko, N.A., Ukhorskiy, A.Y., Brandt, P.C., 2008. Dynamical data-based modeling of the storm-time geomagnetic field with enhanced spatial resolution. J. Geophys. Res.: Space Pol. 113, A07218.

Ukhorskiy, A.Y., Sitnov, M.I., Sharma, A.S., Papadopoulos, K., 2002. Global and multiscale aspects of magnetospheric dynamics in local-linear filters. J. Geophys. Res.: Space Pol. 107. SMP 15–1–SMP 15–18. 1369.

Ukhorskiy, A.Y., Sitnov, M.I., Sharma, A.S., Papadopoulos, K., 2004. Global and multi-scale features of solar wind-magnetosphere coupling: from modeling to forecasting. Geophys. Res. Lett. 31, L08802.

Vassiliadis, D., 2006. Systems theory for geospace plasma dynamics. Rev. Geophys. 44.

Zakharova, A., Loos, S., Siebert, J., Gjurchinovski, A., Claussen, J.C., Schöll, E., 2016. Controlling chimera patterns in networks: interplay of structure, noise, and delay in control of self-organizing nonlinear systems. In: Schöll, P.H.E., Klapp, S.H.L. (Eds.), Control of Self-organizing Nonlinear Systems. Springer, Berlin, Heidelberg, pp. 35–72.

Zhelavskaya, I.S., Spasojevic, M., Shprits, Y.Y., Kurth, W.S., 2016. Automated determination of electron density from electric field measurements on the Van Allen Probes spacecraft. jrnl:14 121, 4611–4625. 2015JA022132.

Zwanzig, R., 2001. Nonequilibrium Statistical Mechanics. Oxford University Press.